Distinguishing antiferromagnetic spin sublattices via the spin Seebeck effect

Yongming Luo, Changjiang Liu, Hilal Saglam, Yi Li, Wei Zhang, Steven S.-L. Zhang, John E. Pearson, Brandon Fisher, Tiejun Zhou, Anand Bhattacharya, and Axel Hoffmann

Phys. Rev. B **103**, L020401 — Published 6 January 2021

DOI: 10.1103/PhysRevB.103.L020401

Distinguishing antiferromagnetic spin sublattices via the spin Seebeck effect

Yongming Luo[1,2†], Changjiang Liu[2†], Hilal Saglam[2], Yi Li[2], Wei Zhang[3], Steven S.-L. Zhang [2,4], John E. Pearson[2], Brandon Fisher[2], Tiejun Zhou[1], Anand Bhattacharya[2*] and Axel Hoffmann[2,5*]

1 School of Electronics and Information, Hangzhou Dianzi University, Hangzhou, Zhejiang, 310018, China.

2 Materials Science Division, Argonne National Laboratory, Argonne, Illinois 60439, USA

3 Department of Physics, Oakland University, Rochester, MI 48309, USA

4 Department of Physics, Case Western Reserve University, Cleveland, Ohio 44106, USA

5 Department of Materials Science and Engineering, University of Illinois at Urbana-Champaign, Urbana, Illinois 61801, USA

† *Yongming Luo and Changjiang Liu contribute equally to this work*

**Corresponding to Axel Hoffmann (axelh@illinois.edu) and Anand Bhattacharya (anand@anl.gov)*

We measured spin Seebeck signals at the top and bottom surfaces of an antiferromagnetic Cr_2O_3 film, using a Pt/Cr_2O_3/Pt tri-layer. Our experimental data, combined with micromagnetic simulations, clearly demonstrate that the uncompensated sublattice at the top and bottom surfaces plays an decisive role in determining the symmetry of the spin Seebeck signals, providing fundamental insights for understanding the generation of spin Seebeck signal in antiferromagnetic materials.

Recently, antiferromagnetic (AF) materials have become of interest for spin transport applications, where they offer the advantages of zero stray fields, robustness against external field, THz dynamics, and abundance of available materials. Recent studies have demonstrated many intriguing phenomena in AF materials, including anisotropic magnetoresistance [1], anomalous Hall effects [2], anomalous Nernst effects [3],spin Hall effects giving rise to spin-orbit torques [4,5], and electrical manipulation of the Néel vector [6]. These developments make AF materials promising for the next generations of spin-based technologies [7-11]. Towards this end, the ability to generate, transport, and detect spin currents in AF insulators have been the focus of recent studies [12]. The transport of spin current in insulators can be realized in the form of magnon currents without associated Joule heating; thus magnon based devices may have the potential to carry and propagate information with low power dissipation [13,14]. Recent studies have demonstrated that AF materials are ideal media to excite and propagate magnons. AF magnons can be excited both thermally [15,16] and resonantly [17]. AF magnon can carry spin information over a few tens of micros [18] and can be switched on or off by manipulating the AF states [19]. Theory also predicts that antiferromagnets may support spin super-fluidity [20]. Therefore, AF insulators have become promising candidates for magnon based devices.

The spin Seebeck effect (SSE) [21-23] provides an ideal platform to study magnon-related phenomena. The SSE occurs in a magnetic/non-magnetic bilayer. A temperature gradient in the magnetic layer $\vec{\nabla} T$ generates a magnon current $\vec{J_s}$ carrying spin angular momentum $\vec{\sigma}$, flowing along $\vec{\nabla} T$. This spin current is injected into the adjacent non-magnetic layer, and if that layer has strong spin-orbit coupling (such as Pt, W), the spin current will subsequently be converted into a measurable electrical voltage through the inverse spin Hall effect. The associated voltage V_{SSE} is given by:

$$V_{SSE} \propto \rho L_v \theta_{SH} (\vec{\mathrm{J}_s} \times \vec{\sigma}) \tag{1}$$

Here, θ_{SH} is the spin Hall angle of the heavy metal layer, ρ is the resistivity of the nonmagnetic later, and L_v is the separation between the electrodes for the voltage measurement. Although the generation of SSE in AF insulators has been demonstrated several years ago [15,16], its microscopic origin is still not well understood. Theoretically, both surface [24] and bulk [25,26] mechanisms for SSE of AF materials have been proposed. But experimentally this issue remains unresolved.

Recently, Gray *et al.* have demonstrated that the SSE is sensitive to the surface sublattice [27]. They developed a magnetothermal microscopy to image the magnetic state in NiO. They found the SSE signal is much larger for uncompensated surfaces than for compensated surface. Based on the fact that the temperature gradient is dominant at the Pt/NiO interface when using use picosecond laser as a heating source, their results indicate that the contrast in SSE images is due to the surface SSE in AF materials, and is determined by the extra sublattice at the uncompensated surface. However, it should be noted that the ultra-fast laser pulse could also result in various other magneto-optical effects [28]. For example, it has been established that the uncompensated surface of NiO (111) could induce larger collinear magnetic difference-frequency generation than other compensated surfaces, which can also contribute to electrical signals [29, 30]. Thus, a direct characterization of the relationship between the surface sublattice and SSE signals, still needs to be established, but remains challenging to realize experimentally. Due to the unavoidable existence of atomic steps and surface roughness, the uncompensated surface of a normal AF material will have the last extra surface sublattices distributed randomly. The coexistence of two antiparallel sublattices makes it difficult to establish a qualitative relationship between the surface sublattice and the SSE signal.

In our work, we avoid the coexistence of two surface sublattices by using Cr_2O_3. The spin-polarized (0001) surface of Cr_2O_3 provides an ideal system to characterize the relationship between the surface sublattice and the SSE signal [31]. We measured the SSE signals at the top and bottom surfaces of Cr_2O_3. We find the SSE signals at opposite surfaces exhibit distinguishable angular dependent symmetry, which is in direct contrast with results in Pt/YIG/Pt structure, where the signature at the top and bottom surfaces are identical [32]. Combined with micromagnetic simulation, we found the distinguishable SSE signal at the top and bottom represent the individual magnetic response of the two antiparallel sublattices in Cr_2O_3, providing a qualitative demonstration of the role of the surface spins in controlling the SSE signal.

Figure 1(A) illustrates the configuration of the Cr_2O_3 (0001) surface. The antiparallel Cr^{3+} ion spins align along the c-axis (z-direction). Within an AF domain at the (0001) surface, the Cr^{3+} ion spins are parallel aligned even with surface steps, exhibiting a long-range magnetic order. Besides, due to the different relative positions with respect to the O^{2-} ions, the Cr^{3+} spins at the top and bottom surfaces are opposite, which represent the two different sublattices. This unique spin structure is due to the requirements of charge-neutrality and the nature of interlayer antiferromagnetic coupling in Cr_2O_3 [31].

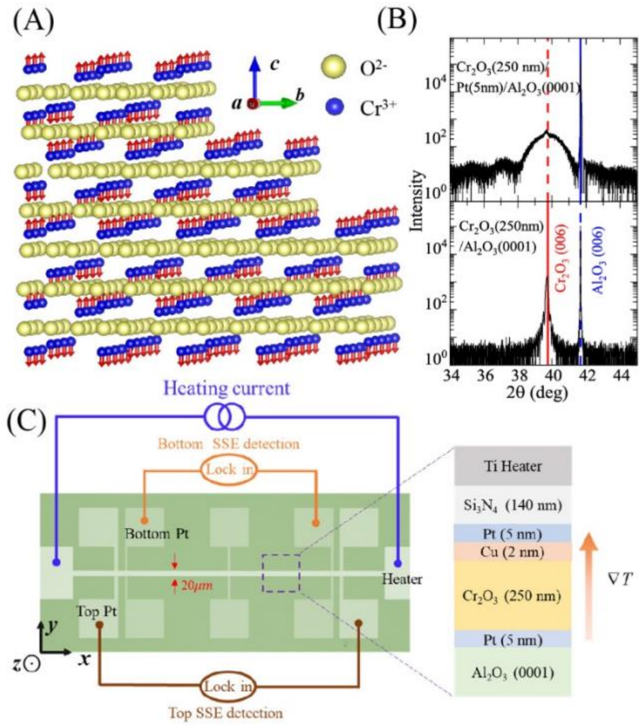

Fig.1 (A) Illustration of the spin structure of a Cr_2O_3 single crystal with a stepped (0001) surface. The red arrows point along the *c* axis denote the spin direction of Cr^{3+} ions. (B) θ-2θ X-ray diffraction pattern of a 180-nm Cr_2O_3 film (lower panel) and Cr_2O_3 (180 nm)/Pt(5 nm) bilayer (upper panel), respectively. The films are deposited on Al_2O_3 (0001) substrates. (C) Experimental setup of the SSE measurements. The left figure is the top view of the device. The insert on the right shows the cross-section of the sample structure.

The Cr_2O_3 film is grown by reactive magnetic sputtering. Figure 1(B) shows the X-ray diffraction (XRD) of a 180-nm Cr_2O_3 layer grown on an Al_2O_3 (0001) substrate with and without Pt bottom layer. The red and blue lines are the standard (0006) peak positions for Cr_2O_3 and Al_2O_3, respectively [33]. Cross-sectional transmission electron microscopy (TEM) images also show that Cr_2O_3 is an epitaxial single-crystal (see the Supplemental Material for details [34]).

FIG. 1 (C) summarizes the sample structure and experiment set-up. We grow a Pt(5 nm)/Cu(2 nm)/Cr_2O_3(180 nm)/Pt(5 nm) layer stack. Here the insertion of 2-nm Cu at the top Pt/Cr_2O_3 interface avoids possible proximity effects [35] and detrimental interfacial anisotropies[36]. The films are patterned into 800 μm × 20 μm Hall-bar structures for transport measurement, as shown in the left panel of Fig. 1(C). In order to provide a temperature gradient during the SSE measurements, we deposit a Ti/ Si_3N_4 layer on top of the film stack, to serve as a resistive heater. The resistance between the top Pt and Ti, and between the top and bottom Pt layer is larger than 20 MΩ at 100 K, demonstrating the good electrical insulation of Si_3N_4 and Cr_2O_3. The right panel of Fig. 1(C) shows a cross-section of the sample structure (see the Supplemental Material for details [34]).

During the measurement, we send a sinusoidal current (3 Hz) through the Ti heater ($P_{heating}$ ~ 5 mWrms), which generates a temperature gradient $\vec{\nabla}T$ normal to the film plane. The resulting V_{SSE} at the top and bottom Pt layers are measured using lock-in techniques at the second harmonic. We apply magnetic fields with different amplitudes in the *y*-*z* plane, as shown in the inset of Fig 1(C).

Figure 2 shows the angular dependence of the SSE signals at different applied magnetic fields at 100 K. We observe a transition at 7.5 T. Below 7.5 T, the SSE voltages at the top and bottom surfaces do not show hysteresis when the field is rotated from 0° to 360° and rotated back from 360° to 0°, while a clear hysteresis appears above that. The rotational symmetry also changes across the transition field. At fields below 7.5 T, the signals at the top and bottom are antisymmetric about $\theta_H = 180^\circ$. While after the transition, the signals before and after $\theta_H = 180^\circ$ exhibit a 180° phase shift and sign reversal. In the simulation part, we demonstrated that this transition is due to the spin flop transition. The spin flop field for bulk Cr_2O_3 is about 6.5 T, while in our thin films, it shifts to 7.5 T, this may due to the strain that exists in the epitaxial film. Another important observation is that the SSE signals at the top and bottom surfaces can be clearly distinguished. Both before and after the transition, the rotational SSE signals from the two surfaces exhibit different shapes, with maxima in their amplitudes realized at different field directions. The distinguishable SSE signals at the different surfaces are in direct contrast to the identical SSE signals at the top and bottom surfaces of ferromagnetic material [32].

The magnitude of the SSE signal is proportional to the heating power (see the Supplemental Material for details [34]), suggesting the thermoelectric nature of the signal. By performing the thermometry at the top and bottom Pt layers [32], the temperature difference across the Cr_2O_3 is determined as $\left|\vec{\nabla}T\right| = 0.043\,K$ at 100 K. The similar rotational symmetry and the transition behavior can be observed between 70 K and 200 K (see the Supplemental Material for details [34]). At the top surface, the signals are qualitatively the same as those that we measured at the bottom surface, even with the insertion of 2-nm Cu. This indicates the spin current generated in the AF can cross through Cu and convert to a charge current in Pt. The measured signals are dominated by SSE and any contribution of the Nernst effect is negligible.

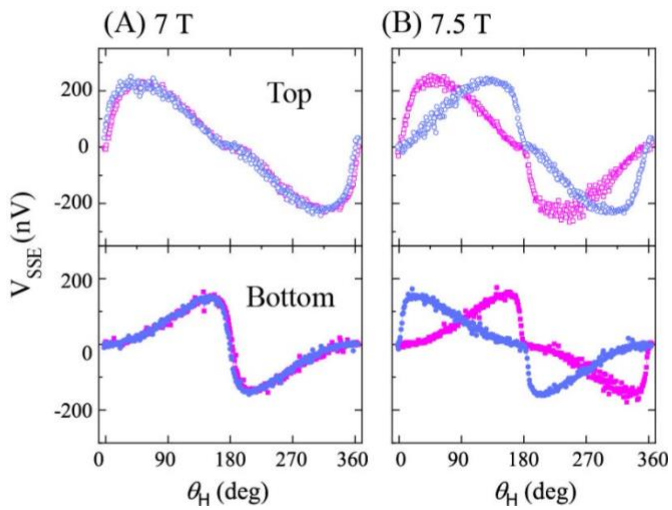

Fig. 2 Angular dependence of the SSE voltages at the top and bottom surfaces of Cr_2O_3 at different fields. In (A) and (B), The upper figures represent the signals measured at the top Pt layer, while the lower figures represent the signals measured at the bottom Pt layer. The magenta and light blue colors represent the signals when the field rotate 0°→ 360° and back 360°→0°, respectively. The temperature during these measurements was 100 K.

We notice the SSE amplitudes at the top surface are larger than at the bottom, even with the insertion of Cu. This is mainly due to the different Pt resistances at the top and bottom, see Eq. (1). The resistance of the top Pt, even with the Cu insertion layer, is higher than that of the bottom Pt, resulting in the larger amplitude of SSE (see the Supplemental Material for details [34]). The resistance difference between the two Pt layers is presumably due to the different roughness or microstructure when Pt is grown on the Al_2O_3 substrate and Cr_2O_3.

To better understand the SSE signal, we simulated the magnetic response of Cr_2O_3 at different fields. Considering Cr_2O_3 is a layered antiferromagnet along the *c*-axis [(0001) plane], we model our system with 30 magnetic layers, with magnetic moments ferromagnetically coupled in the same layer, while antiferromagnetically coupled between adjacent layers. Considering the different microstructure (with Cu insertion at the top surface) and morphologies at the top and bottom surface, we slightly reduce the anisotropy at the top surface (see the Supplemental Material for details [34]). We simulate the angular dependence of the sublattice moments at fields below (6 T) and above the spin-flop transition (8 T). Fig. 3 (A) and (G) plot the angular dependence of the in-plane magnetization component (m_y) at the top surface ($m_y^{i=30}$), bottom surface ($m_y^{i=1}$) , and the net magnetization $\sum_{i=1}^{30} m_y^i$, when 6 T and 8 T magnetic fields are applied in the *y*-*z* plane. Fig. 3 (B)-(E) and (G)-(K) plot the magnetization configurations at selected field orientations.

The simulation results at a 6 T field are plotted in Fig. 3 (A-E). When the field rotates in the *y*-*z* plane, the sublattices tilt from the easy axis, resulting in an in-plane component m_y . As shown in Figs. 3(B), (C), and (D), due to the locally different effective fields, the two sublattices exhibit different line shapes of $m_y^{i=1}$ and $m_y^{i=30}$, and different value of θ_H for the maxima SSE amplitudes. At 6 T field the sublattices only tilt from the easy axis, which is reversible when the field rotates clockwise and counterclockwise.

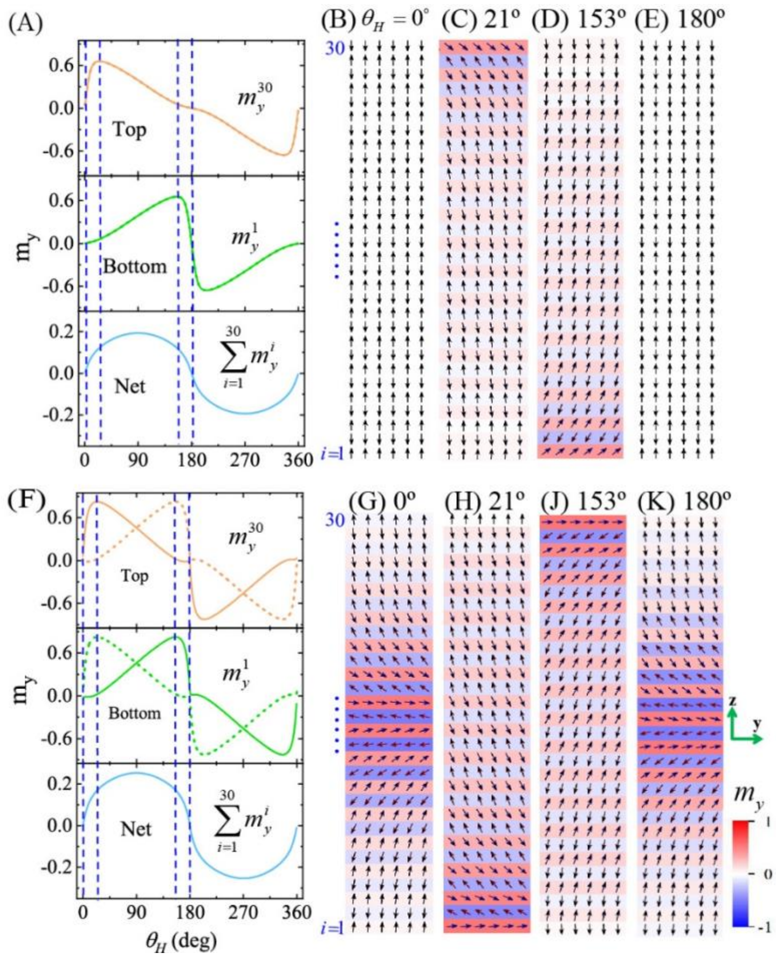

Fig. 3. Simulation of the angular magnetic field dependence of the sublattice moments at 6 T and 8 T, respectively. In (A) and (F), from top to down, are plots of the normalized m_y at the bottom surface ($m_y^{i=1}$), top surface ($m_y^{i=30}$), and the net moment ($\sum_{i=1}^{30} m_y^i$). The sold and dash lines represent the field rotate 0°→ 360° and rotate back 360°→0°, respectively. The blue dashed lines are guidelines for the selected field angles θ_H, at which the magnetization configurations are plotted, as (B) – (E) and (G) – (J) show. The small arrows in (B) – (E) and (G) – (J) indicate the sublattices in each layer. The colors denote m_y, as shown in the color bar. The number on the left side of (B) and (F) denote the layer number i.

When the 8-T field is applied along the easy axis, the magnetic configuration transforms into a non-uniform state, as shown in Fig. 3(G), the top and bottom surfaces are parallel with the field, with a domain wall located in the center of the stack. This is known as a surface spin flop transition and has been studied extensively theoretically and experimentally [37,38]. This phenomenon origin from the reduced coordination at the AF surfaces, where the sublattices at the top and bottom surfaces of an AF film have decreased exchange coupling. When a magnetic field is applied, the surface sublattice that is antiparallel with the field flips first, and then penetrates into the bulk, leading to non-uniform spin states from the center to the surface. The initial domain wall thickness is determined by the exchange coupling and anisotropy, and we estimated this for Cr_2O_3 to be about 4.4 nm. This sets the minimum length-scale for the spin-flopped domain wall, which with increasing magnetic field will extend throughout the whole thickness of the Cr_2O_3 [37, 38]. Rotating the magnetic field in the *y*-*z* plane results in a motion, annihilation, and nucleation of the domain wall, accompanied by the flipping of the sublattices. The flip of the sublattices changes the rotational symmetry of surface sublattices $m_y^{i=1}$ and $m_y^{i=30}$ compared to that at 6 T field (see the Supplemental Material for details [34]).

A direct comparison of the simulation results in Fig. 3 with the SSE voltages in Fig. 2 shows that the direction of the surface sublattices moments dominates the SSE signal. On the other hand, the bulk magnetic order (net moment) is not correlated with the experimentally observed angular dependence of the SSE signals. Therefore, our results qualitatively establish the relationship between the surface sublattice and the SSE in AF materials. Furthermore, our methods can help to distinguish different antiparallel spin states in Cr_2O_3. Fig. 4 show the angular dependence of the SSE signals for two different antiparallel spin states. The distinguishable line shapes at the top and bottom help to distinguish the individual sublattice direction at the surfaces, and further the different antiparallel spin states in uniaxial antiferromagnets. This finding allows us to directly probe electrically and independently the individual sublattices in an antiferromagnet via simultaneously measuring spin Seebeck effects at opposite surfaces. To our knowledge, apart from techniques that probe individual spin in antiferromagnets directly (such as spin-polarized scanning tunneling microscopy), there are few other techniques that can provide independent information for each sublattice independently.

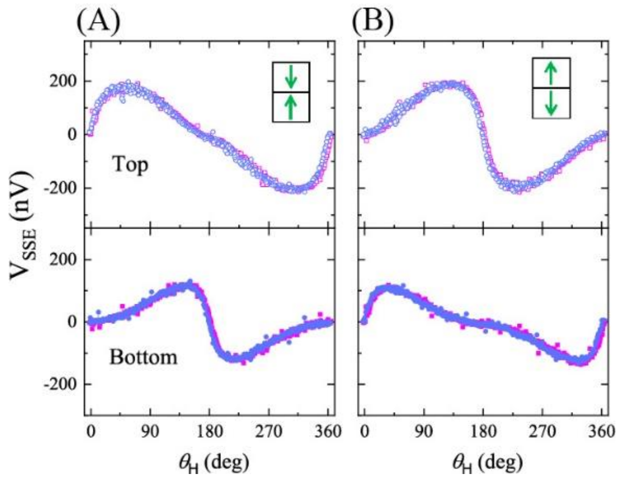

Fig.4 Distinguishing opposite sublattice configuration in uniaxial Cr_2O_3. (A) and (B) show the angular dependence of the SSE signals at the top and bottom surfaces with opposite initial sublattice directions, indicated by the insets. The temperature during the measurements was 100 K. The field amplitude is 6 T.

It is possible that multi-domains with opposite surface sublattices could exist in the devices. To study the influence of a multi-domain state, we simulate the angular dependence of M_y with different degrees of multi-domain states, i.e., different percentages of M_A and M_B (see the Supplemental Material for details [34]). We find the line shape of M_y change from non- sinusoidal to sinusoidal when the degree of multi-domains increases. The non-sinusoidal line shape observed in our samples indicates that the multi-domain states are low (M_B below 10%) and most of the top and bottom sublattices rotate coherently with the field. However, in devices without Cu inserted at the top surface, the line shape at the top surface exhibits sinusoidal behavior (see the Supplemental Material for details [34]), this indicates the insert of Cu may also influence surface anisotropies, which makes the top sublattice easy to be manipulated by field.

In previous experiments, an ultrafast laser pulse was used as the heating source, by which the temperature gradient $\vec{\nabla}T$ is dominated at the Pt/AF interface [27] and concomitantly the surface sublattices play a dominating role in determining the SSE signal. In contrast, in our study, we use low-frequency AC current (3 Hz) as the heating source, where the $\vec{\nabla}T$ in the bulk of AF material is dominant [27] (see the Supplemental Material for details [34]). Our results further demonstrate that even with the temperature gradient in the bulk of AF material, the SSE is still dominated by the surface sublattices. Given that our simulations suggest a significant rotation of the surface spins with respect to the bulk structure, the question then arises how angular momentum associated with bulk magnon modes gets modified near the interface, and what role the excitations of the interface spins themselves play. Therefore, further theoretical and experimental work will be necessary to understand the magnon current driven by temperature gradient and resulting spin currents in the interfacial region.

In conclusion, we qualitatively characterize the relationship between the sublattices and the SSE signals, demonstrating the role of interface spin sublattices in determining the symmetry and hysteretic behavior, which can shed light on understanding the various surface sensitive SSE behaviors [17].

Acknowledgement

This work, including sample fabrication, transport measurements, numerical simulations, and data analysis, was supported by the U. S. Department of Energy, Office of Science, Basic Energy Sciences, Materials Science and Engineering Division. T. J. Zhou acknowledges the support from National Natural Science Foundation of China (11874135) for transmission electron microscopy imaging. Work by S. S.-L. Zhang on the revised manuscript was supported by the College of Arts and Sciences, Case Western Reserve University. We acknowledge Z.-Z. Zhang and V. Novosad for helpful discussion and help.

References

[1]. X. Marti, I. Fina, C. Frontera, J. Liu, P. Wadley, Q. He, R. J. Paull, J. D. Clarkson, J. Kudrnovský, and I. Turek, Nat. Mater. 13, 367 (2014).

[2]. S. Nakatsuji, N. Kiyohara, and T. Higo, Nature 527, 212 (2015).

[3]. M. Ikhlas, T. Tomita, T. Koretsune, M. Suzuki, D. Nishio-Hamane, R. Arita, Y. Otani, and S. Nakatsuji., Nat. Phys. 13, 1085 (2017).

[4]. W. Zhang, M. B. Jungfleisch, W. Jiang, J. E. Pearson, A. Hoffmann, F. Freimuth, and Y. Mokrousov, Phys. Rev. Lett. 113, 196602 (2014).

[5]. S. Fukami, C. Zhang, S. DuttaGupta, A. Kurenkov, and H. Ohno, Nat. Mater. 15, 535 (2016).

[6]. P. Wadley, B. Howells, J. Železný, C. Andrews, V. Hills, R. P. Campion, V. Novák, K. Olejník, F. Maccherozzi, and S. S. Dhesi, Science 351, 587 (2016).

[7]. V. Baltz, A. Manchon, M. Tsoi, T. Moriyama, T. Ono & Y. Tserkovnyak, Rev. Mod. Phys. 90, 015005 (2018).

[8]. T. Jungwirth, X. Marti, P. Wadley, & J. Wunderlich, Nat. Nanotech. 11, 231 (2016).

[9]. Z. Železný, P. Wadley, K. Olejník, A. Hoffmann & H. Ohno, Nat. Phys. 14, 220 (2018).

[10]. M. B. Jungfleisch and W. Zhang & A. Hoffmann, Phys. Lett. A 382 (13), 865 (2018).

[11]. S. A. Siddiqui, J. Sklenar, K. Kang, M. J. Gilbert, A. Schleife, N. Mason, and A. Hoffmann, J. Appl. Phys. 128 (4), 40904 (2020).

[12]. D. Hou, Z. Qiu, and E. Saitoh, NPG Asia. Matter. 11, 1 (2019).

[13]. A. V. Chumak, V. I. Vasyuchka, A. A. Serga, and B. Hillebrands, Nat. Phys. 11, 453 (2015).

[14]. S. D. Bader, and A. Hoffmann, Phys. Rev. Appl. 4, 47001 (2015).

[15]. S. Seki, T. Ideue, M. Kubota, Y. Kozuka, R. Takagi, M. Nakamura, Y. Kaneko, M. Kawasaki, and Y. Tokura, Phys. Rev. Lett. 115, 266601 (2015).

[16]. S. M. Wu, W. Zhang, KC. A, P. Borisov, J. E. Pearson, J. S. Jiang, D. Lederman, A. Hoffmann, and A. Bhattacharya, Phys. Rev. Lett.116, 097204(R) (2016).

[17]. J. Li, C. B. Wilson, R. Cheng, M. Lohmann, M. Kavand, W. Yuan, M. Aldosary, N. Agladze, P. Wei, and M. S. Sherwin, and J. Shi, Nature 578 (7793), 70 (2020).

[18]. R. Lebrun, A. Ross, S. A. Bender, A. Qaiumzadeh, L. Baldrati, J. Cramer, A. Brataas, R. A. Duine, and M. Klaui, Nature 561, 222 (2018)

[19]. J. Han, P. Zhang, Z. Bi, Y. Fan, T. S. Safi, J. Xiang, J. Finley, L. Fu, R. Cheng, and L. Liu, Nat. Nanotechnol. 15, 563 (2020).

[20]. S. Takei, B. I. Halperin, A. Yacoby, and Y. Tserkovnyak, Superfluid spin transport through antiferromagnetic insulators. Phys. Rev. B 90, 94408 (2014).

[21]. K. Uchida, S. Takahashi, K. Harii, J. Ieda, W. Koshibae, K. Ando, S. Maekawa, and E. Saitoh, Nature 455, 778 (2008).

[22]. C. M. Jaworski, J. Yang, S. Mack, D. D. Awschalom, J. P. Heremans, and R. C. Myers, Nat. Mater. 9, 898 (2010).

[23]. K. Uchida, J. Xiao, H. Adachi, J. Ohe, S. Takahashi, J. Ieda, T. Ota, Y. Kajiwara, H. Umezawa, and H. Kawai, Nat. Mater. 9, 894 (2010).

[24]. S. A. Bender, H. Skarsvåg, A. Brataas, and R. A. Duine, Phys. Rev. Lett. 119, 56804 (2017).

[25]. J. Holanda, D. S. Maior, O. Alves Santos, L. H. Vilela-Leão, J. B. S. Mendes, A. Azevedo, R. L. Rodríguez-Suárez, and S. M. Rezende, Appl. Phys. Lett. 111,172405 (2017).

[26]. R. L. Rodríguez-Suárez, A. Azevedo and S. M. Rezende, Phys. Rev. B 93, 014425 (2016).

[27]. Gray, T. Moriyama, N. Sivadas, G. M. Stiehl, J. T. Heron, R. Need, B. J. Kirby, D. H. Low, K. C. Nowack, and D. G. Schlom, Phys. Rev. X 9, 41016 (2019).

[28]. P. Němec, M. Fiebig, T. Kampfrath, and A. V. Kimel, Nat. Phys. 14, 229 (2018).

[29]. H. Qiu, et al., Nat. Phys. (2020). https://doi.org/10.1038/s41567-020-01061-7.

[30]. T. Higuchi, N. Kanda, H. Tamaru, and M. Kuwata-Gonokami, Phys. Rev. Lett. 106, 47401 (2011).

[31]. X. He, Y. Wang, N. Wu, A. N. Caruso, E. Vescovo, K. D. Belashchenko, P. A. Dowben, and C. Binek, Nat. Mater. 9, 579 (2010).

[32]. Uchida, T. Kikkawa, A. Miura, J. Shiomi, and E. Saitoh, Phys. Rev. X 4, 41023 (2014).

[33]. Y. Shiratsuchi, Y. Takechi, K. Toyoki, Y. Nakano, S. Onoue, C. Mitsumata, and R. Nakatani, Applied Physics Express, 6(12), 123004 (2013).

[34]. See Supplemental Material at [URL], for the sample fabrication, the TEM image of sample cross section, the temperature dependent SSE measurements, heating power dependence of SSE signals, the estimation of the temperature gradient, influence of the multi-domain states, the role of Cu insertion, the influence of Cr_2O_3 on Pt Hall signal and simulation details.

[35]. B. F. Miao, S. Y. Huang, D. Qu, C. L. Chien. AIP Advances, 6(1), 015018 (2016).

[36]. Y. Shiratsuchi et al., J. Appl. Phys. 121, 073902 (2017)
[37]. R. W. Wang, D. L. Mills, E. E. Fullerton, J. E. Mattson, and S. D. Bader, Phys. Rev. Lett. 72, 920 (1994).
[38]. D. L. Mills, Phys. Rev. Lett. 20, 18 (1968).